

Article

In-Vitro Degradation of Hollow Silica Reinforced Magnesium Syntactic Foams in Different Simulated Body Fluids for Biomedical Applications

Vyasaraj Manakari ¹, Sathish Kannan ², Gururaj Parande ¹, Mrityunjay Doddamani ³, Soumya Columbus ², Priya Sudha K ⁴, S. Vincent ⁴ and Manoj Gupta ^{1,*}

¹ Department of Mechanical Engineering, National University of Singapore, 9 Engineering Drive 1, Singapore 117576, Singapore; mbvyasaraj@u.nus.edu (V.M.); gururaj.parande@u.nus.edu (G.P.)

² Department of Mechanical Engineering, American University of Sharjah, Sharjah 26666, UAE; skannan@aus.edu (S.K.); soumyacolumbus@gmail.com (S.C.)

³ Advanced Manufacturing Laboratory, Department of Mechanical Engineering, National Institute of Technology Karnataka, Surathkal 575025, India; mrdoddamani@nitk.edu.in

⁴ Department of Mechanical Engineering, BITS Pilani, Dubai Campus, Dubai 345055, UAE; priyasudha32@gmail.com (P.S.K.); vincent@dubai.bits-pilani.ac.in (S.V.)

* Correspondence: mpegm@nus.edu.sg; Tel.: +65-65166358

Received: 10 October 2020; Accepted: 24 November 2020; Published: 26 November 2020



Abstract: This article reports the mechanical and biocorrosion behaviour of hollow silica nanosphere (SiO₂) reinforced (0.5–2 vol.%) magnesium (Mg) syntactic foams. Room temperature tensile properties' characterization suggests that the increased addition of hollow silica nanospheres resulted in a progressive increase in tensile yield strength (TYS) and ultimate tensile strength (UTS) with Mg-2 vol.% SiO₂ exhibiting a maximum TYS of 167 MPa and a UTS of 217 MPa. The degradation behaviour of the developed Mg-SiO₂ syntactic foams in four different simulated body fluids (SBFs): artificial blood plasma solution (ABPS), phosphate-buffered saline solution (PBS), artificial saliva solution (ASS) and Hanks' balanced saline solution (HBSS) was investigated by using potentiodynamic polarization studies. Results indicate that corrosion resistance of the Mg-SiO₂ syntactic foam decreases with increasing chloride ion concentration of the SBF. Mg-1.0 vol.% SiO₂ displayed the best corrosion response and its corrosion susceptibility pertaining to corrosion rate and polarisation curves in different SBF solutions can be ranked in the following order: ABPS > PBS > HBSS > ASS. The surface microstructure demonstrated the presence of a better passivated layer on the syntactic foams compared to pure Mg. The observed increase in corrosion resistance is correlated with intrinsic changes in microstructure due to the presence of hollow silica nanospheres. Further, the effect of corrosive environment on the degradation behaviour of Mg has been elucidated.

Keywords: magnesium; silica nanosphere; syntactic foam; mechanical behaviour; simulated body fluid; biocorrosion

1. Introduction

Benefitting from the advantages of being bioresorbable and having an elastic modulus, density and mechanical properties that closely match load bearing bones, magnesium (Mg)-based materials are emerging to play a crucial role in both basic research and clinical applications for orthopaedic and craniofacial fracture fixation [1,2]. Moreover, Mg²⁺ ions, the main degradation product of Mg-based materials, are essential for many biological activities as they participate in over 300 enzymatic reactions, formation of apatite and bone cell adsorption [3]. In addition, Mg-based materials have demonstrated low thrombogenicity, good osteoinduction and antibacterial properties compared to traditionally

used permanent metallic implants made of titanium (Ti) alloys or stainless steel [4,5]. Further, these permanent metallic implants often result in stress-shielding at bone–implant interface due to mismatch in elastic modulus, osteolysis due to toxic metal ion release during wear and corrosion, tissue tear and other clinical complications during removal surgeries [6–8]. Collectively, Mg-based bioresorbable implants can be superior alternatives for temporary fracture fixation applications eliminating the need for revision surgeries following the healing of damaged tissues, thereby reducing the burden on patients and healthcare system.

However, low corrosion resistance of Mg in physiological environments has greatly limited its widespread clinical applicability [1]. Rapid release of degradation products cause a sharp rise in local pH accumulating alkaline ions and H₂ gas bubbles leading to premature decline of mechanical strength and adversely influencing the cellular functions and cytocompatibility [3,9]. Therefore, it is imperative to tailor the strength and degradation properties of Mg for successful clinical translation and various approaches like alloying [10], heat treatments [11], surface modifications [12], bioactive coatings [13] and nanocomposite development [6] have been adopted to overcome these challenges. Though alloying has been one of the effective approaches to enhance mechanical behaviour and corrosion resistance to Mg, commonly used alloying elements like aluminium and rare-earth elements have been known to cause adverse effects on the human body in long term including haemolysis, neurotoxicity and hepatotoxicity [3,10,14]. Further, alternative strategies of surface modification and bioactive coating have not endowed long lasting corrosion resistance in case of biodegradable metal like Mg [15]. Poor coating quality due to residual defects (cracks and porosity) can result in rapid propagation of pits leading to speeding up the Mg-based materials corrosion during sustained aggressive electrolytes exposure containing Cl⁻, SO₄²⁻ and HCO₃⁻ ions [16,17].

A further promising strategy is to reinforce biocompatible nano-length scale reinforcements (<3 vol.%) into Mg matrix for controlling the degradation without compromising the mechanical response [18]. Synergistic strengthening mechanisms like Orowan, Hall–Petch, Forest and Taylor strengthening help in simultaneously improving the mechanical and corrosion performance of the nanocomposites [18,19]. For example, Parande et al. reported that reinforcing hydroxyapatite (HAP) nanoparticles (NPs) into an Mg alloy resulted in nanocomposite exhibiting superior mechanical properties than commercially available Mg-alloys such as WE43, AZ31, ZK21 and AZ91 [6]. In addition, the presence of nano-HAP as a reinforcement helped in minimizing pitting corrosion while improving the biocompatibility and cell attachment of the nanocomposite. In addition to HAP, various other metal oxide NPs like Sm₂O₃, CeO₂, ZnO, ZrO₂ and TiO₂ have also been reinforced with Mg to achieve superior mechanical and corrosion performance owing to their high chemical stability, high degree of biocompatibility and non-toxicity [18,20,21].

Metal matrix composites developed by reinforcing hollow particles are termed as “syntactic foams” wherein the hollow reinforcement particles impart porosity into metal matrix using a closed cell structure. Literature survey reveals no previous attempt made so far to study the detailed effect of nano-scale hollow particles on the mechanical and in-vitro degradation behaviour of magnesium syntactic foams. If the nano-scale gas pores are introduced into the Mg matrix, the pore size is smaller than the critical dimension of cracks which already exist in the matrix, then the material density could be reduced while maintaining the essential mechanical properties. Hollow SiO₂ NPs are extensively researched in biomedical applications such as biosensors [22], enzyme supporters [23], controlled drug release and delivery and cellular uptake [24,25]. In addition, hollow SiO₂ NPs have high specific surface area, low density, good biocompatibility and low toxicity [26,27]. In a recent study, Yu et al. [28] observed that hollow SiO₂ NPs exhibited no signs of toxicity and could be safely metabolized and tolerated in mice without longstanding cytotoxicity signifying the potential of SiO₂ NPs in developing magnesium-based nanocomposites for temporary fracture fixation applications. Further, in our recent study [29], hollow silica nanospheres reinforced magnesium nanocomposites were observed to have positive stimulatory effect on osteoblasts in vitro with significant improvements in cell adhesion and proliferation compared to pure Mg.

Hence, in this study, hollow silica (SiO₂) nanospheres (10–20 nm) were chosen as a reinforcement to develop Mg-SiO₂ syntactic foams. The developed syntactic foams were evaluated for mechanical and in-vitro degradation behaviour for potential use as temporary implant materials. To the best of the authors' knowledge, this is the first comparative investigation on bio-corrosion behaviour of a Mg-syntactic foam in four different simulated body fluids (SBF) to elucidate the effect of corrosive environment on the degradation behaviour of Mg.

2. Materials and Methods

Mg-SiO₂ syntactic foams having pure Mg (purity 99.9%, Acros Organics, Waltham, MA, USA) and 0.5, 1.0, 1.5 and 2.0 volume percent silica (SiO₂) nanospheres (~10–20 nm size range and purity > 99.2%, Sigma Aldrich, Singapore) were prepared using the Disintegrated Melt Deposition (DMD) approach [18]. Cylindrical ingots (Φ 40 mm) obtained from DMD were machined into billets (Φ 36 mm × 45 mm) and subsequently hot extruded with 20.25:1 ratio at 350 °C [29]. Cylindrical rods of Φ 8 mm were obtained and trimmed to required dimensions to perform the mechanical and corrosion experiments.

The grain size analysis of the samples was performed using a Leica optical microscope model DM2500 M (Leica Microsystems (SEA) Pte Ltd., Singapore). An average of 50 grains were used to compute the average grain size of each sample. To reveal the grains, the samples were etched using the etchant: 20 mL acetic acid, 60 mL ethylene glycol, 1 mL nitric acid (Sigma Aldrich, Singapore) and 20 mL distilled water. The morphology of the samples' surface was investigated using JEOL JSM-6010 scanning electron microscope (Jeol USA Inc., Peabody, MA, USA) equipped with EDS. Microhardness measurements were performed on the polished cylindrical specimens (Φ 8 mm × 5 mm) using a Vickers microhardness tester (Shimadzu-HMV, Kyoto, Japan) with 245.5 mN and 15 s, test load and dwell time, respectively. Tests in tensile mode were conducted on dog bone shaped specimen (25 mm gauge length, Φ 5 mm) as outlined in ASTM E8M-01 on MTS 810 at a constant crosshead displacement of 0.254 mm/min corresponding to 0.010 min⁻¹ strain rate. Instron 2630-100 series extensometer (Singapore) is used to measure the fracture strain. Five replicates were tested in each composition and the average values were reported.

Electrochemical measurements in various physiological environments were conducted in a typical three electrode cell (AUTOLAB 204 Potentiostat Galvanostat, Herisau, Switzerland) using a sample as a working electrode, an immersed calomel reference terminal (SCE = 241 mV) and a platinum gage counter anode. Prior to electrochemical measurements, the samples were mechanically polished up to 1200 grit [29], degreased ultrasonically with acetone (Sigma Aldrich, Singapore), rinsed using distilled water and finally pulsed air dried. The working electrode (WE) exposure to the solution was 1 cm², and the open circuit potential was monitored continuously for 30 min. The polarization curves were measured with 0.167 mV/s scan rate and the potential was varied between -100 mV to 100 mV. The following solutions were used as electrolytes: (i) artificial blood plasma (ABP) (pH 7.4), (ii) PBS (pH 7.4), (iii) artificial saliva solution (ASS) (pH 6.2) and (iv) Hanks' balanced saline solution (HBSS) (pH 7.4). All electrolytes were prepared from analytical reagent-grade chemicals using distilled water [30]. Table 1 shows the compositions of the various simulated body fluids used in the present investigation.

Table 1. Chemical compositions of different simulated body fluids.

Contents (g/L)	ABPS	PBS	ASS	HBSS
NaCl	8.036	8.0	1.5	8.0
NaHCO ₃	0.352	-	1.5	0.35
NaH ₂ PO ₄	-	1.15	0.5	-
KCl	0.225	0.2	-	0.4
KSCN	-	-	0.5	-
KH ₂ PO ₄	-	0.2	-	0.06
Lactic Acid	-	-	0.9	-
Na ₂ HPO ₄ ·3H ₂ O	0.238	-	-	-
MgCl ₂ ·6H ₂ O	0.311	-	-	-
CaCl ₂	0.293	-	-	-
Na ₂ SO ₄	0.0072	-	-	-
CaCl ₂ ·2H ₂ O	-	-	-	0.19
MgSO ₄ ·7H ₂ O	-	-	-	0.2
Na ₂ HPO ₄ ·7H ₂ O	-	-	-	0.09
Glucose	-	-	-	1.0

3. Results and Discussion

Uniform distribution of the hollow silica nanospheres was observed in the Mg matrix (Figure 1) with good interfacial integrity and minimal agglomeration even for the highest SiO₂ addition. This can be due to the optimized processing conditions of casting and extrusion [29]. Earlier efforts on Mg-nanocomposites have shown that the presence of uniformly dispersed nano sized reinforcements would actively pin the grain boundaries and assist in nucleation of grains [31]. As evident in the micrographs of Mg-SiO₂ in Figure 1, the distribution of reinforcing particles is fairly homogeneous in Mg. The evidence of SiO₂ at the grain boundaries together with its distribution pattern provides effective pinning mechanism for reducing the grain size significantly from 27 to 10.5 μm (Table 2) [31].

Table 2. Results of grain size measurements and tensile properties of pure Mg and Mg-SiO₂ syntactic foams.

Material	Grain Size (μm)	Microhardness (Hv)	0.2 TYS (MPa)	UTS (MPa)	Fracture Strain (%)
Pure Mg	27 ± 1	59 ± 1	103 ± 5	148 ± 6	7.9 ± 0.5
Mg-0.5SiO ₂	23 ± 3 (↓14.8%)	73 ± 2 (↑23.7%)	133 ± 3 (↑29.1%)	181 ± 1 (↑22.3%)	6.7 ± 0.2 (↓15.2%)
Mg-1.0SiO ₂	15 ± 3 (↓44.4%)	83 ± 2 (↑40.7%)	145 ± 2 (↑40.8%)	198 ± 7 (↑33.8%)	5.7 ± 0.2 (↓27.8%)
Mg-1.5SiO ₂	13 ± 4 (↓51.9%)	89 ± 1 (↑50.8%)	152 ± 1 (↑47.5%)	203 ± 3 (↑37.2%)	5.2 ± 0.2 (↓34.2%)
Mg-2SiO ₂	10 ± 2 (↓61%)	92 ± 1 (↑55.9%)	167 ± 4 (↑62.1%)	217 ± 7 (↑46.7%)	4.7 ± 0.3 (↓40.5%)
Cortical bone	-	-	104–114	35–283	1.07–2.10
Cancellous bone	-	-	-	1.5–38	-

(↓x%) and (↑x%) indicates the percentage decrease and increase in the property with respect to pure Mg by x%, respectively.

The microhardness results of the pure Mg and Mg-SiO₂ syntactic foams are shown in Table 2. The progressive additions of hollow silica nanospheres resulted in a steady increase in the hardness values of pure Mg. With the addition of 2 vol.% SiO₂, a maximum hardness value of ~92 Hv was observed which is ~56% greater than that of pure Mg. This increasing trend in the hardness values can be attributed to the constraint to localized deformation due to the presence of high hardness SiO₂ NPs (750 Hv) [32], near-uniform distribution of silica nanospheres within the Mg matrix and the reduced grain size of the syntactic foams [33].

Room temperature tensile behaviour of Mg and Mg-SiO₂ syntactic foams are presented in Table 2 and stress-strain response is graphed in Figure 2. The incorporation of hollow silica nanospheres into Mg led to progressive improvement in both 0.2% tensile yield strength (TYS) and ultimate tensile strength (UTS) whereas the tensile failure strain exhibited declining trend (Table 2). Mg-2 vol.% SiO₂

registered the maximum TYS and UTS values of 167 and 217 MPa, respectively that are ~62 and 46% higher than that of pure Mg.

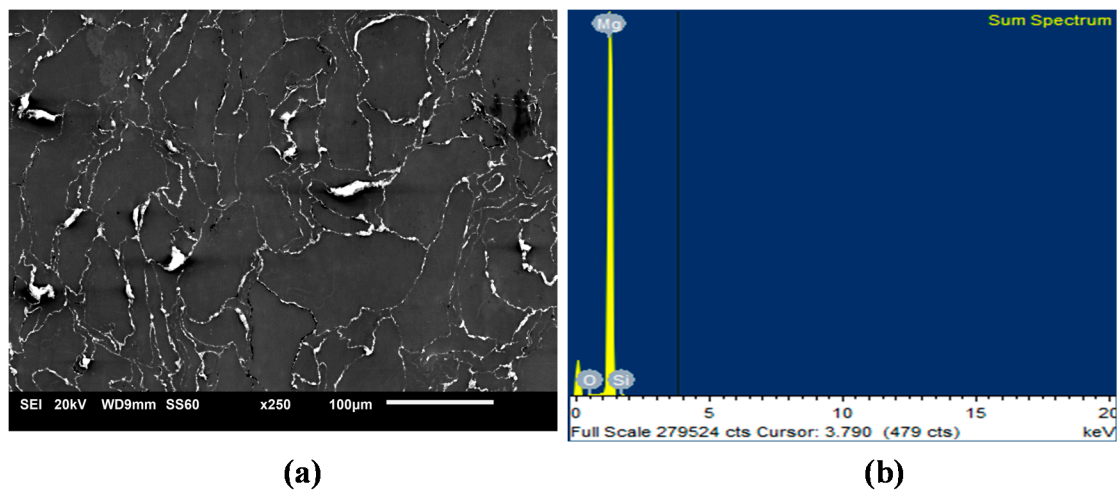


Figure 1. Representative micrographs of (a) SiO_2 distribution and (b) EDS sum spectrum in representative Mg-1.0 SiO_2 .

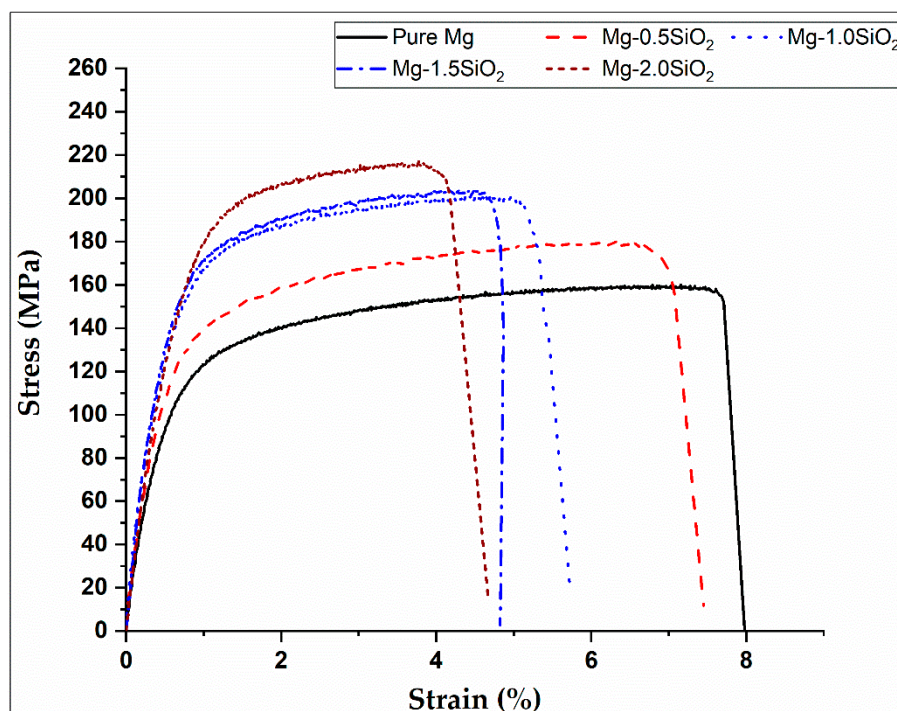


Figure 2. Stress–strain graphs of Mg and Mg- SiO_2 syntactic foams.

Strength improvement might be due to the finer grains in Mg- SiO_2 leading to grain boundary strengthening based on the Hall-Petch relationship. Additionally, effective load transfers due to homogenous SiO_2 distribution in Mg matrix and higher dislocation density because of CTE and modulus differences between Mg and hollow silica nanospheres might be the reasons for such an observation. The failure strain decreases gradually with increasing hollow silica nanosphere content in Mg- SiO_2 syntactic foams. Similar failure strain reductions in for nanocomposites has been reported in literature with the addition of ceramic reinforcements [18]. A minimum ductility of 4.7% was noted in Mg-2 SiO_2 syntactic foam. However, for implants in biomedical applications, a minimum fracture

strain of 5% is desired [34]. Therefore, only Mg-0.5SiO₂ and Mg-1.0SiO₂ syntactic foams were further analysed for in-vitro degradation behaviour in different simulated body fluids.

Figure 3 shows the Tafel curves of Mg and Mg-SiO₂ syntactic foams after immersing them in different SBF solutions and the corresponding electrochemical parameters extracted from them are listed in Table 3. The corrosion potential for pure Mg was the lowest generally. Hollow silica nanosphere addition resulted in corrosion potentials shift towards the noble direction along with reduction in the anodic kinetics in artificial blood plasma solution (ABPS), HBSS and ASS medium. This indicates increased corrosion resistance for the syntactic foams. It is interesting to observe that anodic regions of Mg-0.5SiO₂ and Mg-1.0SiO₂ demonstrating passive regions in all the SBF media, implying that the dissolution process was effectively hindered in syntactic foams when compared to pure Mg. The significant grain refinements observed in the syntactic foams due the presence of hollow silica nanospheres enables their surface to passivate more readily by breaking down the secondary phase particles along the grain boundary and subsequently improving their corrosion performance [35].

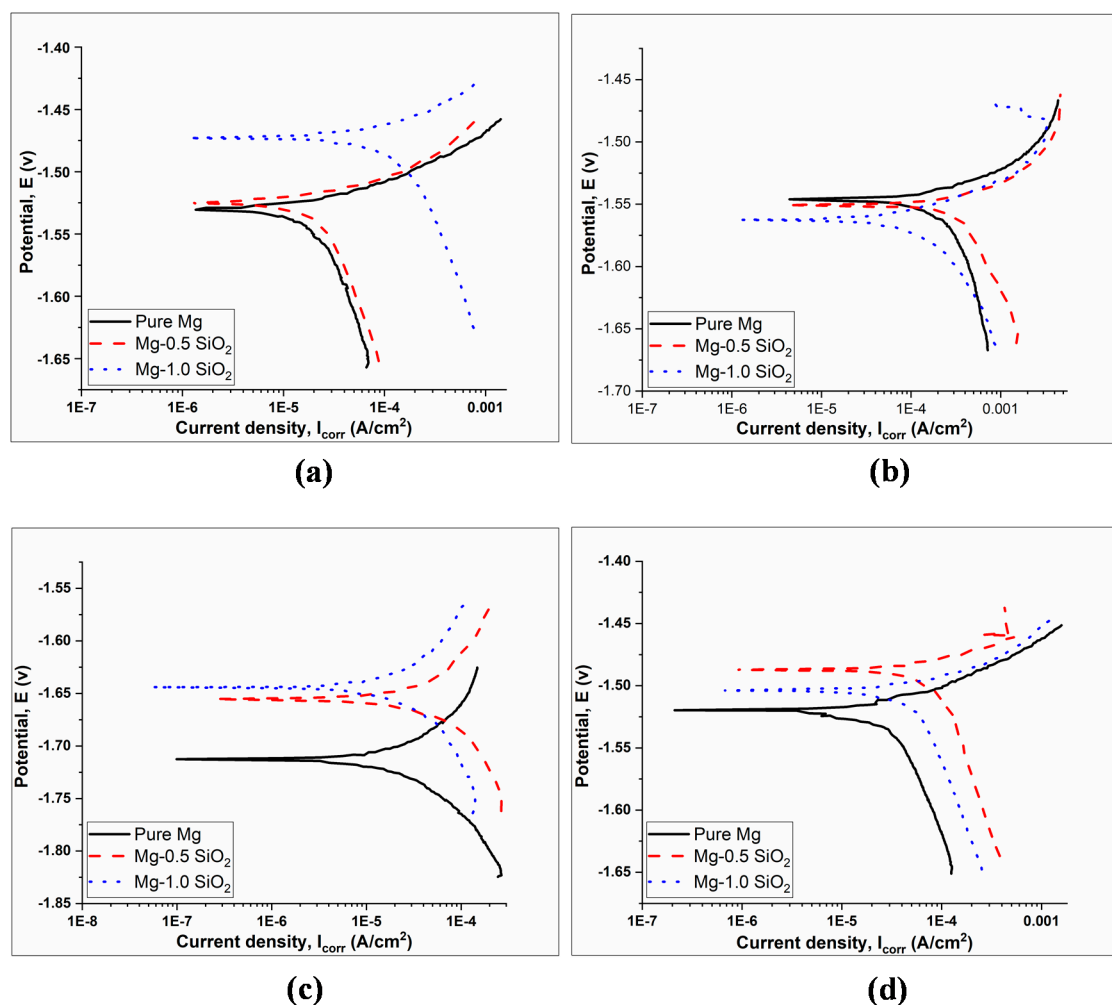


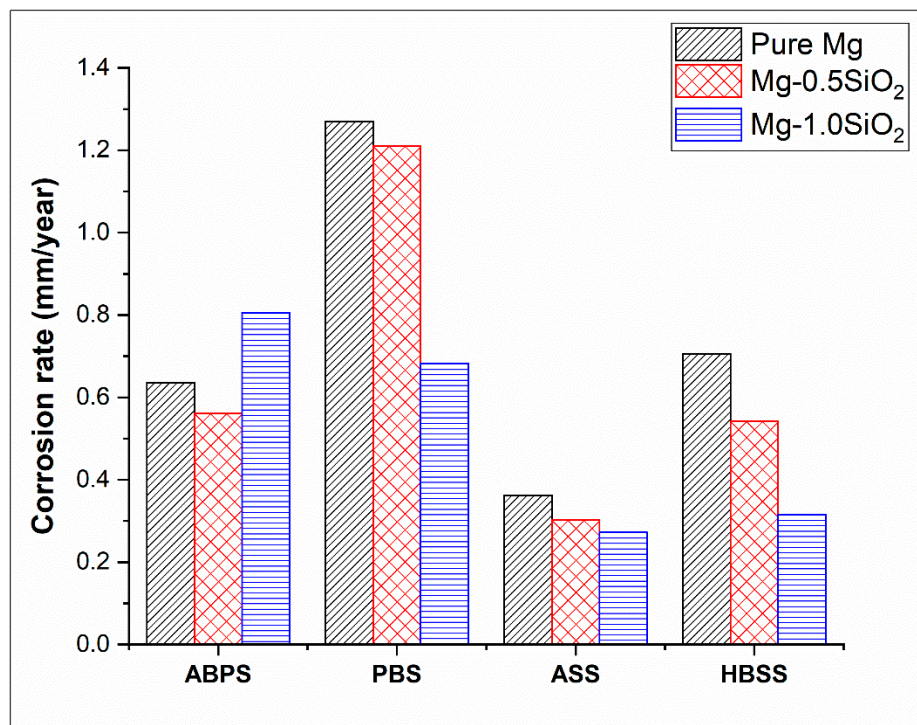
Figure 3. Polarization curves for pure Mg and Mg-SiO₂ syntactic foams in (a) artificial blood plasma solution (ABPS), (b) phosphate-buffered saline solution (PBS), (c) artificial saliva solution (ASS) and (d) Hanks' balanced saline solution (HBSS) mediums.

The corrosion rate of Mg and their syntactic foams was estimated in different SBF and presented in Figure 4. The corrosion rates in mm/year were calculated using i_{corr} with the help of Faraday's Law using the following equation [36]:

$$\text{Corrosion Rate (mm/year)} = 3.27 \times 10^{-3} \times i_{\text{corr}} (\mu\text{A/cm}^2) \quad (1)$$

Table 3. Corrosion current density (i_{corr}) and potential (E_{corr}) of Mg-SiO₂ in simulated body fluids (SBFs).

Type of Solution	Material	i_{corr} ($\mu\text{A}/\text{cm}^2$)	E_{corr} (V vs. SCE)
ABPS	Pure Mg	27.77	-1.53
	Mg-0.5SiO ₂	24.45	-1.52
	Mg-1.0SiO ₂	35.05	-1.48
PBS	Pure Mg	55.46	-1.54
	Mg-0.5SiO ₂	52.76	-1.55
	Mg-1.0SiO ₂	29.67	-1.55
ASS	Pure Mg	15.83	-1.72
	Mg-0.5SiO ₂	13.15	-1.66
	Mg-1.0SiO ₂	11.85	-1.65
HBSS	Pure Mg	30.82	-1.52
	Mg-0.5SiO ₂	23.61	-1.48
	Mg-1.0SiO ₂	13.71	-1.50

**Figure 4.** Corrosion rate in Mg-SiO₂ syntactic foams in SBFs.

Mg-1.0SiO₂ syntactic foam displayed the best corrosion response overall (except for ABPS) and its corrosion susceptibility pertaining to corrosion rate and polarisation curves in different SBF solutions can be ranked in the following order: ABPS > PBS > HBSS > ASS. As per the earlier reports, an implant is required to have a maximal degradation rate of 0.5 mm/year in simulated body fluid [37]. Mg-1.0SiO₂ syntactic foam was found to have lower corrosion rate than 0.5 mm/year in both HBSS (0.32 mm/year) and ASS (0.27 mm/year) medium, whereas Mg-0.5SiO₂ syntactic foam exhibited a corrosion rate of 0.54 and 0.3 mm/year in HBSS and ASS medium, respectively. The most crucial factors that govern the corrosion behaviour of Mg-based material systems in an aqueous environment are chemical compositions of the SBF and their pH. It has been shown that a physiological pH (7.2–7.4) can drastically accelerate magnesium dissolution [38]. The present study also demonstrates that APBS, PBS and HBSS with pH 7.4 impart higher corrosion to the synthesized materials compared to ASS which has a pH of 6.2. Further, higher concentration of chloride ions (Cl⁻) plays a significant role in accelerating the corrosion of Mg by pitting mode [39]. Likewise, sulphate ions (SO₄²⁻) also increase

dissolution of Mg but to the lesser extent compared to Cl^- ions [39]. Amongst ABPS, PBS and HBSS having the same pH of 7.4, it was observed that ABPS mediated corrosion was more pronounced than that of PBS and HBSS for Mg-1.0SiO₂ syntactic foam. It can be observed from Table 1 and Figure 4 that, increased presence of Cl^- and SO_4^{2-} ions in ABPS compared to PBS and HBSS accelerate the dissolution process in Mg-1.0SiO₂ syntactic foam. Interestingly high corrosion rate is observed in PBS (Figure 4) for pure Mg and Mg-0.5SiO₂ syntactic foam compared to all other electrolytic solutions, though PBS is having low chemical composition (Table 1). It has been reported that an increase in dihydrogen phosphate (NaH_2PO_4 , KH_2PO_4) increases H₂ evolution rate in Mg-based materials [39]. From Table 1, it can be observed that concentration of dihydrogen phosphate is highest in PBS in comparison to other electrolytic solutions. This could be possible reason for high corrosion rate in PBS. In addition, it should be noted that the Mg-SiO₂ syntactic foams exhibit lowest corrosion rates in HBSS compared to PBS and ABPS which can be attributed to the formation of more pronounced Ca-P apatite layer on the sample surface due to the presence of glucose [40].

Surface microstructure of corroded samples after polarization experiment was analysed using SEM (Figures 5–7). Figure 5 shows the morphology of surface and corresponding EDS of pure Mg and Mg-1.0SiO₂ in ABPS medium. Many cross-linked cracks are clearly visible on the surface as a result of dehydration during SEM sample preparation [41,42]. A protective layer with few pits can be seen on the surface of pure Mg (Figure 5). However, the presence of hollow silica nanospheres has decreased the extent of pitting in the syntactic foams. The EDS mapping results of the sample reveal higher amounts of Mg, O and P and lower Ca contents. This in turn imply the formation of magnesium and calcium-based phosphate compounds which assist in the apatite layer formation. Results also show a more uniform and denser passive layer formation for the Mg-1.0SiO₂ syntactic foam (Figure 5b) compared to Mg. The layer formation process is expedited by the presence of hollow silica nanospheres as it provides a favourable environment for the sample in the immersive medium. Such a layer delays onset of corrosion as it acts as a barrier between the matrix and the immersive medium, resulting in improved corrosion resistance for the syntactic foams [43]. Further, the precipitation of uniformly distributed hollow silica nanospheres can provide impermeability of the Mg matrix, preventing rapid release of H₂ gas in the physiological environment [44].

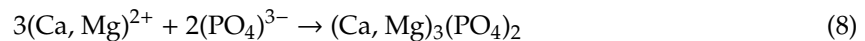
The degradation of Mg-based materials in Cl^- ion containing ABPS, PBS and HBSS solutions is influenced by the ionic interactions between Mg^{2+} , Cl^- , OH^- in the SBF as presented in the following equations [45]:



Initially, when the Mg and Mg-SiO₂ syntactic foams are immersed into the SBF solutions, anodic dissolution of Mg leads to Mg^{2+} ions release which interact with the alkaline OH^- ions forming a protective hydroxide ($\text{Mg}(\text{OH})_2$) layer. At the same time, Cl^- ions present in the SBF solutions breakdown this protective layer by transforming $\text{Mg}(\text{OH})_2$ to more soluble MgCl_2 by peeling the layer along the grain boundaries. This process is delayed in the Mg-SiO₂ syntactic foams due to the presence of refined grains owing to the nanoparticle addition, thus enhancing corrosion resistance. Further, the dissolution of Mg^{2+} promotes the formation of apatite layer by providing OH^- ions, leading to HPO_4^{2-} and PO_4^{3-} formation.



Thirdly, Ca^{2+} , HPO_4^{2-} and PO_4^{3-} groups present in the SBF solutions react with Mg^{2+} resulting in magnesium and calcium-based phosphate precipitation improving the degradation resistance.



Further, carbonate ions' (HCO_3^-) presence induces rapid surface passivation of Mg because of magnesium carbonates (MgCO_3) precipitation [46]. In the present work, ASS contains higher concentration of HCO_3^- (1500 mg/L). Hence, deposition of magnesium carbonates in corrosive product layer might have contributed positively in lowering the corrosion rate. Moreover, lower pH (6.2) and lesser concentration of chloride ions in ASS result in further reduction in the extent of dissolution in the syntactic foams (Figure 4 and Table 3). Mg-1.0SiO₂ micrography post corrosion in ASS exhibits a surface covered with a dense protective layer compared to pure Mg (Figure 6). Magnified images further demonstrate the thick depositions on the syntactic foams surface might be composed of magnesium carbonates prominent in the case of ASS mediated corrosion. Whereas, in the case of HBSS mediated corrosion, comparably dense passive layer is found on the surface compared to ASS (Figure 7). These dense regions may be due to the deposition of Ca-P compounds which is a characteristic of HBSS mediated corrosion. Yet few bare Mg surface locations were exposed, which act as sites for localized corrosion enhancing magnesium syntactic foams degradation rate in HBSS.

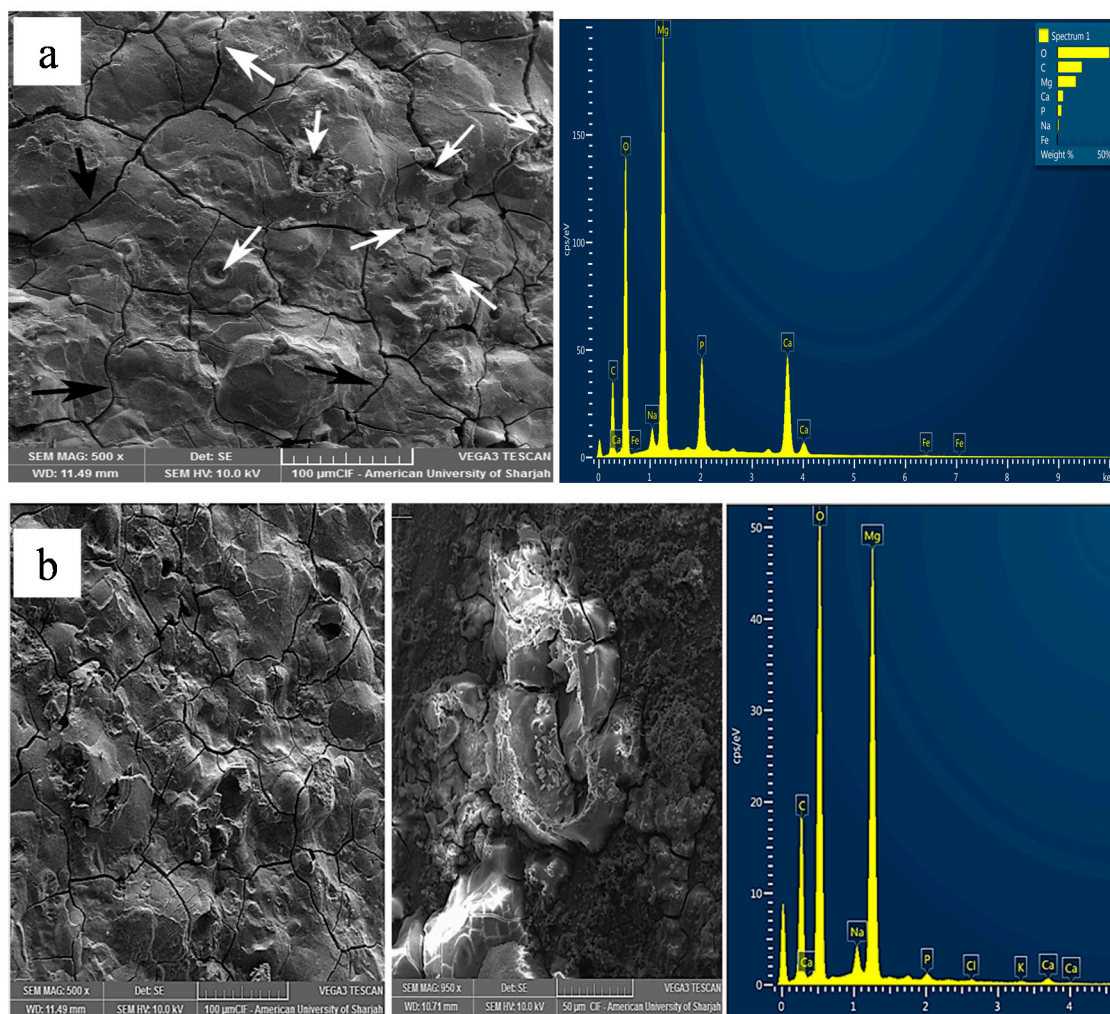


Figure 5. Representative micrographs of corroded surface for (a) pure Mg and (b) Mg-1.0SiO₂ in ABPS medium.

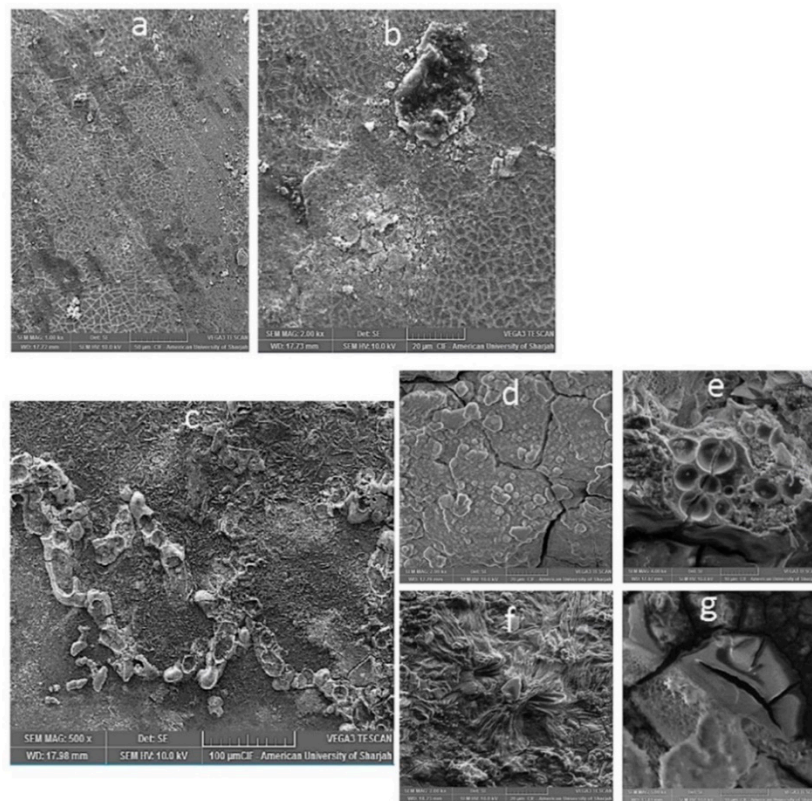


Figure 6. Micrographs depicting corrosion surface morphology. (a,b) Pure Mg in ASS and (c–g) Mg-1.0SiO₂ in ASS (in different area of sample at different magnifications).

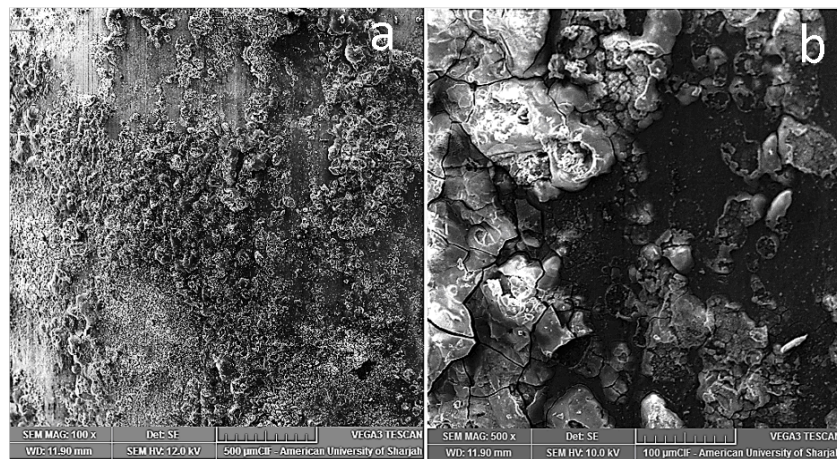


Figure 7. Micrographs depicting corrosion surface morphology. (a,b) Mg-1.0 SiO₂ in HBSS at different magnifications.

Further work is continuing in this area to evaluate the long-term corrosion resistance of the synthesized syntactic foams with additional characterizations such as immersion testing, hydrogen evolution, analysis of the degradation surface and products with energy dispersive spectroscopy (EDS), X-ray diffraction (XRD) and inductively coupled plasma atomic emission spectrometry (ICP-AES) to provide a more holistic view towards clinical translation for biodegradable implant applications.

4. Conclusions

Inspired by the attractive potential of Mg-based nanocomposites in orthopaedic and craniofacial applications, in this study, the influence of hollow silica nanosphere addition on the mechanical and biocorrosion properties of pure Mg were studied.

1. The incorporation of hollow silica nanospheres into Mg led to the progressive enhancement in both 0.2% TYS and UTS whereas the tensile failure strain exhibited declining trend.
2. Corrosion resistance of the Mg-SiO₂ syntactic foams increased with decreasing presence of chloride, sulphate and dihydrogen phosphate concentrations and increasing carbonate concentration.
3. Mg-1.0 vol.% SiO₂ syntactic foam displayed the best corrosion response and its corrosion susceptibility pertaining to corrosion rate and polarisation curves in different SBF solutions can be ranked in the following order: ABPS > PBS > HBSS > ASS.
4. Mg-SiO₂ syntactic foams demonstrated better surface passivation effect which accounts for better corrosion resistance in all the SBF solutions.
5. Surface microstructure analysis showed that the syntactic foams samples maintained structural integrity after corrosion and no significant pitting was observed.

Author Contributions: Conceptualization, V.M. and M.G.; methodology, S.K. and S.V.; software, S.C.; validation, G.P., M.D. and P.S.K.; formal analysis, S.K. and S.V.; investigation, S.C., M.D. and V.M.; resources, M.D., S.V.; writing—original draft preparation, V.M., G.P.; writing—review and editing, M.D. and M.G.; visualization, M.G.; supervision, S.K., S.V. and M.G.; funding acquisition, M.G., and S.K. All authors have read and agreed to the published version of the manuscript.

Funding: This research was funded by Singapore Ministry of Education Academic Research Funding grant number WBS# R-265-000-684-114 and American University of Sharjah, UAE, Research Grant (EFRG18-MSE-CEN20).

Acknowledgments: The authors greatly acknowledge the invaluable contribution of Walid Qureshi in the corrosion testing and analysis.

Conflicts of Interest: The authors declare no conflict of interest.

References

1. Prasad, S.; Ratheesh, V.; Manakari, V.; Parande, G.; Gupta, M.; Wong, R. The potential of magnesium based materials in mandibular reconstruction. *Metals* **2019**, *9*, 302. [[CrossRef](#)]
2. Manakari, V.; Parande, G.; Gupta, M. Selective laser melting of magnesium and magnesium alloy powders: A review. *Metals* **2017**, *7*, 2. [[CrossRef](#)]
3. Aidin, B.-K.; Benyamin, Y.; Masoud, M. Emerging magnesium-based biomaterials for orthopedic implantation. *Emerg. Mater. Res.* **2019**, *8*, 305–319.
4. Yang, G.; Yang, H.; Shi, L.; Wang, T.; Zhou, W.; Zhou, T.; Han, W.; Zhang, Z.; Lu, W.; Hu, J. Enhancing corrosion resistance, osteoinduction, and antibacterial properties by zn/sr additional surface modification of magnesium alloy. *ACS Biomater. Sci. Eng.* **2018**, *4*, 4289–4298. [[CrossRef](#)]
5. Sillekens, W.H. Magnesium-based biodegradable implants. *Emerg. Mater. Res.* **2013**, *2*, 216–218. [[CrossRef](#)]
6. Parande, G.; Manakari, V.; Prasad, S.; Chauhan, D.; Rahate, S.; Wong, R.; Gupta, M. Strength retention, corrosion control and biocompatibility of mg–zn–si/ha nanocomposites. *J. Mech. Behav. Biomed. Mater.* **2020**, *103*, 103584. [[CrossRef](#)]
7. Cipriano, A.F.; Sallee, A.; Guan, R.-G.; Lin, A.; Liu, H. A comparison study on the degradation and cytocompatibility of mg-4zn-x sr alloys in direct culture. *ACS Biomater. Sci. Eng.* **2017**, *3*, 540–550. [[CrossRef](#)]
8. Manakari, V.; Parande, G.; Doddamani, M.; Gupta, M. Enhancing the ignition, hardness and compressive response of magnesium by reinforcing with hollow glass microballoons. *Materials* **2017**, *10*, 997. [[CrossRef](#)]
9. Witecka, A.; Bogucka, A.; Yamamoto, A.; Máthys, K.; Krajčák, T.; Jaroszewicz, J.; Świąszkowski, W. In vitro degradation of zm21 magnesium alloy in simulated body fluids. *Mater. Sci. Eng. C* **2016**, *65*, 59–69. [[CrossRef](#)]
10. Li, T.; He, Y.; Zhou, J.; Tang, S.; Yang, Y.; Wang, X. Effects of scandium addition on biocompatibility of biodegradable mg–1.5 zn–0.6 zr alloy. *Mater. Lett.* **2018**, *215*, 200–202. [[CrossRef](#)]
11. He, R.; Liu, R.; Chen, Q.; Zhang, H.; Wang, J.; Guo, S. In vitro degradation behavior and cytocompatibility of mg-6zn-mn alloy. *Mater. Lett.* **2018**, *228*, 77–80. [[CrossRef](#)]

12. López, A.F.; Lehr, I.L.; Saidman, S.B. Anodisation of az91d magnesium alloy in molybdate solution for corrosion protection. *J. Alloy. Compd.* **2017**, *702*, 338–345. [[CrossRef](#)]
13. Zhang, D.; Qi, Z.; Shen, H.; Wei, B.; Zhang, Y.; Wang, Z. In vitro degradation and cytocompatibility of magnesium alloy coated with hf/plla duplex coating. *Mater. Lett.* **2018**, *213*, 249–252. [[CrossRef](#)]
14. Gu, X.; Zheng, Y.; Cheng, Y.; Zhong, S.; Xi, T. In vitro corrosion and biocompatibility of binary magnesium alloys. *Biomaterials* **2009**, *30*, 484–498. [[CrossRef](#)]
15. Peng, F.; Li, H.; Wang, D.; Tian, P.; Tian, Y.; Yuan, G.; Xu, D.; Liu, X. Enhanced corrosion resistance and biocompatibility of magnesium alloy by mg–al-layered double hydroxide. *ACS Appl. Mater. Interfaces* **2016**, *8*, 35033–35044. [[CrossRef](#)]
16. Aparicio, M.; Mosa, J.; Rodriguez, G.; Guzman, J.; Picard, Q.; Klein, L.C.; Jitianu, A. Consolidated melting gel coatings on az31 magnesium alloy with excellent corrosion resistance in nacl solutions: An interface study. *ACS Appl. Mater. Interfaces* **2018**, *11*, 3493–3505. [[CrossRef](#)]
17. Gu, X.-N.; Li, S.-S.; Li, X.-M.; Fan, Y.-B. Magnesium based degradable biomaterials: A review. *Front. Mater. Sci.* **2014**, *8*, 200–218. [[CrossRef](#)]
18. Gupta, M.; Parande, G.; Manakari, V. An insight into high performance magnesium alloy/nano-metastable-syntactic composites. In Proceedings of the 17th Australian International Aerospace Congress, Melbourne, Australia, 26–28 February 2017; p. 270.
19. Thornby, J.; Verma, D.; Cochrane, R.; Westwood, A.; Manakari, V.; Gupta, M.; Haghshenas, M. Indentation-based characterization of creep and hardness behavior of magnesium carbon nanotube nanocomposites at room temperature. *Sn Appl. Sci.* **2019**, *1*, 695. [[CrossRef](#)]
20. Gupta, M.; Wong, W. Magnesium-based nanocomposites: Lightweight materials of the future. *Mater. Charact.* **2015**, *105*, 30–46. [[CrossRef](#)]
21. Kujur, M.S.; Mallick, A.; Manakari, V.; Parande, G.; Tun, K.S.; Gupta, M. Significantly enhancing the ignition/compression/damping response of monolithic magnesium by addition of sm2o3 nanoparticles. *Metals* **2017**, *7*, 357. [[CrossRef](#)]
22. Tallury, P.; Payton, K.; Santra, S. Silica-based multimodal/multifunctional nanoparticles for bioimaging and biosensing applications. *Future Med.* **2008**. [[CrossRef](#)] [[PubMed](#)]
23. Coll, C.; Mondragón, L.; Martínez-Máñez, R.; Sancenón, F.; Marcos, M.D.; Soto, J.; Amorós, P.; Pérez-Payá, E. Enzyme-mediated controlled release systems by anchoring peptide sequences on mesoporous silica supports. *Angew. Chem. Int. Ed.* **2011**, *50*, 2138–2140. [[CrossRef](#)] [[PubMed](#)]
24. Chu, Z.; Huang, Y.; Tao, Q.; Li, Q. Cellular uptake, evolution, and excretion of silica nanoparticles in human cells. *Nanoscale* **2011**, *3*, 3291–3299. [[CrossRef](#)] [[PubMed](#)]
25. Vivero-Escoto, J.L.; Slowing, I.L.; Trewyn, B.G.; Lin, V.S.Y. Mesoporous silica nanoparticles for intracellular controlled drug delivery. *Small* **2010**, *6*, 1952–1967. [[CrossRef](#)] [[PubMed](#)]
26. Halas, N.J. Nanoscience under glass: The versatile chemistry of silica nanostructures. *ACS Nano* **2008**, *2*, 179–183. [[CrossRef](#)]
27. Qureshi, W.; Kannan, S.; Vincent, S.; Eddine, N.; Muhammed, A.; Gupta, M.; Karthikeyan, R.; Badari, V. Influence of Silica Nanospheres on Corrosion Behavior of Magnesium Matrix Syntactic Foam. *IOP Conf. Ser. Mater. Sci. Eng.* **2018**, *346*, 012012. [[CrossRef](#)]
28. Yu, X.; Yang, K.; Chen, X.; Li, W. Black hollow silicon oxide nanoparticles as highly efficient photothermal agents in the second near-infrared window for in vivo cancer therapy. *Biomaterials* **2017**, *143*, 120–129. [[CrossRef](#)]
29. Prasad, S.; Manakari, V.; Parande, G.; Wong, R.C.W.; Gupta, M. Hollow silica reinforced magnesium nanocomposites with enhanced mechanical and biological properties with computational modeling analysis for mandibular reconstruction. *Int. J. Oral Sci.* **2020**, *12*, 31. [[CrossRef](#)]
30. Vincent, S.; Daiwile, A.; Devi, S.; Kramer, M.; Besser, M.; Murty, B.; Bhatt, J. Bio-corrosion and cytotoxicity studies on novel zr 55 co 30 ti 15 and cu 60 zr 20 ti 20 metallic glasses. *Metall. Mater. Trans. A* **2015**, *46*, 2422–2430. [[CrossRef](#)]
31. Parande, G.; Manakari, V.; Meenashisundaram, G.K.; Gupta, M. Enhancing the tensile and ignition response of monolithic magnesium by reinforcing with silica nanoparticulates. *J. Mater. Res.* **2017**, *32*, 2169–2178. [[CrossRef](#)]
32. Michel, M.D.; Serbena, F.C.; Lepienski, C.M. Effect of temperature on hardness and indentation cracking of fused silica. *J. Non-Cryst. Solids* **2006**, *352*, 3550–3555. [[CrossRef](#)]

33. Lloyd, D. Particle reinforced aluminium and magnesium matrix composites. *Int. Mater. Rev.* **1994**, *39*, 1–23. [[CrossRef](#)]
34. Chandra, G.; Pandey, A. Biodegradable bone implants in orthopedic applications: A review. *Biocybern. Biomed. Eng.* **2020**, *40*, 596–610. [[CrossRef](#)]
35. Ralston, K.; Birbilis, N.; Davies, C. Revealing the relationship between grain size and corrosion rate of metals. *Scr. Mater.* **2010**, *63*, 1201–1204. [[CrossRef](#)]
36. Ison, H.C.K. Handbook on corrosion testing and evaluation. *Br. Corros. J.* **1972**, *7*, 55. [[CrossRef](#)]
37. Bao, L.; Le, Q.; Zhang, Z.; Esling, C. A novel degradation rate controlling mechanism of biocompatible mg-zn-y-zr alloys. *Mater. Lett.* **2019**, *235*, 189–192. [[CrossRef](#)]
38. Johnston, S.; Shi, Z.; Atrens, A. The influence of ph on the corrosion rate of high-purity mg, az91 and ze41 in bicarbonate buffered hanks' solution. *Corros. Sci.* **2015**, *101*, 182–192. [[CrossRef](#)]
39. Zeng, R.-C.; Hu, Y.; Guan, S.-K.; Cui, H.-Z.; Han, E.-H. Corrosion of magnesium alloy az31: The influence of bicarbonate, sulphate, hydrogen phosphate and dihydrogen phosphate ions in saline solution. *Corros. Sci.* **2014**, *86*, 171–182. [[CrossRef](#)]
40. Zeng, R.-C.; Li, X.-T.; Li, S.-Q.; Zhang, F.; Han, E.-H. In vitro degradation of pure mg in response to glucose. *Sci. Rep.* **2015**, *5*, 13026. [[CrossRef](#)]
41. Xin, Y.; Liu, C.; Zhang, X.; Tang, G.; Tian, X.; Chu, P.K. Corrosion behavior of biomedical az91 magnesium alloy in simulated body fluids. *J. Mater. Res.* **2007**, *22*, 2004–2011. [[CrossRef](#)]
42. Xin, Y.; Hu, T.; Chu, P.K. Degradation behaviour of pure magnesium in simulated body fluids with different concentrations of hco₃. *Corros. Sci.* **2011**, *53*, 1522–1528. [[CrossRef](#)]
43. Kujur, M.S.; Manakari, V.; Parande, G.; Tun, K.S.; Mallick, A.; Gupta, M. Enhancement of thermal, mechanical, ignition and damping response of magnesium using nano-ceria particles. *Ceram. Int.* **2018**, *44*, 15035–15043. [[CrossRef](#)]
44. Borisova, D.; Mohwald, H.; Shchukin, D.G. Mesoporous silica nanoparticles for active corrosion protection. *ACS Nano* **2011**, *5*, 1939–1946. [[CrossRef](#)] [[PubMed](#)]
45. Bakhsheshi-Rad, H.R.; Idris, M.H.; Abdul-Kadir, M.R.; Ourdjini, A.; Medraj, M.; Daroonparvar, M.; Hamzah, E. Mechanical and bio-corrosion properties of quaternary mg–ca–mn–zn alloys compared with binary mg–ca alloys. *Mater. Des.* **2014**, *53*, 283–292. [[CrossRef](#)]
46. Wu, G.; Li, P.; Feng, H.; Zhang, X.; Chu, P.K. Engineering and functionalization of biomaterials via surface modification. *J. Mater. Chem. B* **2015**, *3*, 2024–2042. [[CrossRef](#)]

Publisher's Note: MDPI stays neutral with regard to jurisdictional claims in published maps and institutional affiliations.



© 2020 by the authors. Licensee MDPI, Basel, Switzerland. This article is an open access article distributed under the terms and conditions of the Creative Commons Attribution (CC BY) license (<http://creativecommons.org/licenses/by/4.0/>).